

# In vitro and in vivo investigations of upconversion and NIR emitting $\text{Gd}_2\text{O}_3:\text{Er}^{3+}, \text{Yb}^{3+}$ nanostructures for biomedical applications

Eva Hemmer · Hiroyuki Takeshita · Tomoyoshi Yamano · Takanori Fujiki ·  
Yvonne Kohl · Karin Löw · Nallusamy Venkatachalam · Hiroshi Hyodo ·  
Hidehiro Kishimoto · Kohei Soga

Received: 31 October 2011 / Accepted: 2 May 2012 / Published online: 16 May 2012  
© Springer Science+Business Media, LLC 2012

**Abstract** The use of an “over 1000-nm near-infrared (NIR) in vivo fluorescence bioimaging” system based on lanthanide containing inorganic nanostructures emitting in the visible and NIR range under 980-nm excitation is proposed. It may overcome problems of currently used biomarkers including color fading, phototoxicity and scattering.  $\text{Gd}_2\text{O}_3:\text{Er}^{3+}, \text{Yb}^{3+}$  nanoparticles and nanorods showing upconversion and NIR emission are synthesized and their cytotoxic behavior is investigated by incubation with B-cell hybridomas and macrophages. Surface modification with PEG-*b*-PAAc provides the necessary chemical durability reducing the release of toxic  $\text{Gd}^{3+}$  ions. NIR fluorescence microscopy is used to investigate the suitability of the nanostructures as NIR–NIR biomarkers. The in vitro uptake of bare and modified nanostructures by macrophages is investigated by confocal laser scanning

microscopy. In vivo investigations revealed nanostructures in liver, lung, kidneys and spleen a few hours after injection into mice, while most of the nanostructures have been removed from the body after 24 h.

## 1 Introduction

Biocompatible nanomaterials have become the focus of intensive research due to their manifold applications ranging from implants and scaffolds [1–3], drug delivery and controlled release [4–9] to cell-tracking and bioimaging [10, 11]. Bioimaging is an important tool to visualize and investigate biological phenomena and in diagnostics. The early and reliable detection of diseases such as cancer, heart or neural diseases is essential for successful treatment and much effort has been undertaken in the field of nanomedicine [12–14]. Commonly, organic dyes and fluorescent proteins are used as fluorescent markers [15, 16]. Recently, semiconductor quantum dots (e.g. CdSe) have been proposed as biomarkers due to their tunable optical properties [17]. However, organic dyes suffer from color fading restricting their temporal use [15, 18], auto-fluorescence of the biological tissue and phototoxicity as well as scattering when ultraviolet (UV) light is used as excitation source. The main disadvantages of semiconductor quantum dots are their intrinsic toxicity requiring core-shell structures, such as CdTe/ZrO<sub>2</sub> or CdSe/CdS, and the blinking of their luminescence emission [19–21]. Due to their outstanding optical properties, such as sharp emission lines, long lifetimes and photostability, lanthanide (Ln) containing compounds may overcome those drawbacks [22]. In addition to their luminescence behavior, their magnetic properties make Ln-containing compounds promising candidates for bioimaging applications as hybrid

**Electronic supplementary material** The online version of this article (doi:10.1007/s10856-012-4671-x) contains supplementary material, which is available to authorized users.

E. Hemmer (✉) · H. Hyodo · H. Kishimoto · K. Soga  
Center for Technologies Against Cancer (CTC), Tokyo  
University of Science, 2669 Yamazaki, Chiba 278-0022, Japan  
e-mail: eva.hemmer@sogalabo.jp

H. Takeshita · T. Yamano · H. Kishimoto  
Division of Immunobiology, Research Institute for Biological  
Sciences, Tokyo University of Science, 2669 Yamazaki,  
Chiba 278-0022, Japan

T. Fujiki · N. Venkatachalam · H. Hyodo · K. Soga  
Department of Materials Science and Technology, Tokyo  
University of Science, 2641 Yamazaki, Chiba 278-8510, Japan

Y. Kohl · K. Löw  
Department of Cell Biology & Applied Virology, Fraunhofer  
Institute for Biomedical Engineering, Ensheimer Straße 48,  
66386 St. Ingbert, Germany

(opto-magneto) biomarkers [23, 24]. Luminescent rare earth doped gadolinium oxide nanorods exhibiting good T1-weighted MRI contrast have been reported by Tan et al. [25]. Alkaline-earth metal fluoride nanocrystals doped with  $Gd^{3+}$  have been proposed by Pang et al. as bifunctional biomarkers due to their magnetism and luminescence [26]. Ceramic host materials doped with erbium ions are known as upconverting (UPC) phosphors that absorb near-infrared (NIR) radiation and emit in the visible spectrum. Synthesis of poly(ethylene glycol)/streptavidin coimmobilized upconverting  $Y_2O_3:Er^{3+},Yb^{3+}$  nanophosphors and their potential as biomarkers have been reported by our own group [27]. Xiong et al. [28] described peptide-labeled  $NaYF_4: 20\%Yb, 1.8\%Er, 0.2\%Tm$  nanophosphors for the in vivo imaging of tumors. Herein, main advantages of NIR light are the reduced phototoxicity, autofluorescence and scattering when compared to UV light. Reduced scattering allows a deeper penetration depth into biological tissue due to its NIR transparency also known as biological window [29]. However, the use of NIR to visible upconverting biomarkers still suffers from the reduced penetration depth and scattering of the emitted visible light. Therefore, NIR absorbing and NIR emitting inorganic materials as well as organic compounds are attracting increasing attention and are expected to be suitable nanoprobe for in vivo bioimaging. Hilderbrand et al. [30] reported the successful application of  $Y_2O_3$  nanoparticles modified with NIR emitting fluorophores as NIR–NIR biomarkers. Prasad et al. [31] reported in vivo bioimaging of whole-body animal by use of  $Tm^{3+}/Yb^{3+}$  co-doped  $NaYF_4$ . Further,  $Gd^{3+}$  and  $Er^{3+}/Yb^{3+}/Eu^{3+}$  doped  $NaYF_4$  and  $Tm^{3+}/Er^{3+}/Yb^{3+}$  co-doped  $NaGdF_4$  nanocrystals have been suggested as bifunctional bioprobes due to their NIR–NIR emission and magnetic resonance properties [32–34]. With regards to clinical application NIR–NIR biomarkers are suitable image-guidance tools in surface-near (millimeter range) surgery as shown by Frangioni et al. [35, 36]. Using a fluorescence microscope equipped with an InGaAs-CCD liposome-encapsulated  $Y_2O_3:Er^{3+}$  nanostructures emitting NIR fluorescence at 1,550 nm under 980-nm excitation have been investigated for in vitro analysis by Soga et al. [37]. For further evaluation of the potential of biomarkers based on Ln-ions, which efficiently emit in the over-1000-nm NIR range, an “over-1000-nm NIR in vivo fluorescence bioimaging” (OTN-NIR-IFBI) system consisting of a 980-nm laser diode with a scanner for the fluorescence excitation and an InGaAs-CCD, which can detect the image in between 800 and 1,700 nm, was developed by our group. NIR fluorescence microscopy is used for in vitro cellular imaging on a micron scale level. In contrast, the new OTN-NIR-IFBI system allows not only in vitro but also in vivo imaging on a micron to millimeter scale including investigations of, e.g. uptake of nanostructures

by organs, their in vivo distribution or their suitability as new markers in cell tracking.

Previously, we reported the preparation of bare and poly(ethylene glycol)-*b*-poly(acrylic acid) (PEG-*b*-PAAc) modified  $Gd_2O_3:Er^{3+},Yb^{3+}$  nanostructures and the investigation of their in vitro cytotoxicity by incubation with B-cell hybridomas and macrophages [38]. While no cytotoxic effect was observed towards B-cell hybridomas, bare nanostructures induced a toxic effect on macrophages. This observation was deduced to the poor chemical durability of  $Gd_2O_3$  and formation of toxic  $Gd^{3+}$  when the nanostructures are uptaken by macrophages. Surface modification with PEG-*b*-PAAc provided the necessary chemical durability resulting in good in vitro biocompatibility. In the present study, the effect of PEG-*b*-PAAc modification on the in vitro cellular up-take of gadolinium oxide nanostructures by macrophages was investigated by confocal laser scanning microscopy (CLSM) using the upconversion emission of  $Gd_2O_3:Er^{3+},Yb^{3+}$  under 980-nm excitation. Further, the in vivo distribution of PEG-*b*-PAAc modified  $Gd_2O_3:Er^{3+},Yb^{3+}$  nanorods by hydrothermal synthesis ( $l/d \sim 5$ ) and nanoparticles ( $d \sim 85\text{--}210$  nm) by homogeneous precipitation (HP) method was evaluated. Herein, the imaging was performed by using the lately developed “1000-nm NIR in vivo fluorescence bioimaging” (OTN-NIR-IFBI) system.

## 2 Materials and methods

### 2.1 Material synthesis

Starting materials like lanthanide nitrates [Ln = Gd (min. 99.95 %, Kanto Chemical Co., Inc., Tokyo, Japan), Er (>99 %, Kojundo Kagaku Kenkyusho Co., Japan), Yb (99.9 %, Kojundo Kagaku Kenkyusho Co., Japan)], urea (min. 99.0 %, Kanto Chemical Co., Inc., Tokyo, Japan), PEG-6.000 [poly(ethylene glycol), Mw = 6,000, Kanto Chemical Co., Inc., Tokyo, Japan], cetyltrimethylammonium bromide (CTAB, Wako Pure Chemical Industries, Ltd., Osaka, Japan), ammonia (25 % aqueous solution, Kanto Chemical Co., Inc., Tokyo, Japan), and poly(ethylene glycol)-*b*-poly(acrylic acid) [PEG-*b*-PAAc block copolymer, Mw = 5,000/3,200, Polymersource, Dorval (Montreal), Canada] were used without further purification.

For HP, 1.68 mmol  $Gd(NO_3)_3 \cdot 6H_2O$ , 1 mol%  $Er(NO_3)_3 \cdot 5H_2O$  and 1 mol%  $Yb(NO_3)_3 \cdot xH_2O$  were dissolved in 300 mL  $H_2O$ . As surfactant either 1–10 mmol CTAB or 1–10 mmol CTAB and 5 mmol PEG-6.000 were added, followed by stirring for 50 min at room temperature. 150 mmol urea were added to the pure Ln- or Ln-surfactant-solution and the mixture was kept stirring for 10 min. For precipitation, the mixture was stirred at 85 °C

for 30 min. In hydrothermal synthesis (HT), the concentration of gadolinium nitrate was set to 0.05 mol/L at a total volume of 30 mL. Therefore, 1.5 mmol  $\text{Gd}(\text{NO}_3)_3 \cdot 6\text{H}_2\text{O}$  and an appropriate amount of  $\text{Er}(\text{NO}_3)_3 \cdot 5\text{H}_2\text{O}$  and  $\text{Yb}(\text{NO}_3)_3 \cdot x\text{H}_2\text{O}$  (each 1 mol%) were dissolved in 9 mL  $\text{H}_2\text{O}$  and quickly added to an aqueous ammonia solution (1 mL ammonia hydroxide aqueous solution, 25 %, +20 mL  $\text{H}_2\text{O}$ ) under rigorous stirring. After enclosing the Teflon liners in steel autoclaves, autoclaves were placed in a furnace, respectively wrapped into a heating mantle system (equipped with a thermocouple K:Class:2 by Toho and a Program Temperature Controller TXN700 by AS ONE) and heated to a temperature of 200 °C that was kept for 6–12 h. In all cases, the obtained powders were collected by centrifugation, washed two times with distilled water and dried at 80 °C for at least 12 h. Crystalline oxide powders were obtained by post-thermal treatment at 900 °C (30 min).

## 2.2 Surface modification

For surface modification of  $\text{Gd}_2\text{O}_3:\text{Er}^{3+}, \text{Yb}^{3+}$  with PEG-*b*-PAAc, the nanostructures were dispersed in water ( $c = 2 \text{ mg/mL}$ ) and sonicated for 30 min at room temperature. An aqueous PEG-*b*-PAAc solution was added into the nanostructure dispersion, resulting in final concentrations of 0.6 mg/mL  $\text{Gd}_2\text{O}_3:\text{Er}^{3+}, \text{Yb}^{3+}$  and 0.6 or 1.2 mg/mL PEG-*b*-PAAc. In case of 0.6 mg/mL PEG-*b*-PAAc, 6 mg/mL PEG-6.000 have been added to the aqueous nanostructure dispersion prior to addition of the PEG-*b*-PAAc solution in order to increase viscosity of the reaction mixture hindering the formation of larger agglomerates. The mixtures were stirred at 35 °C for 24 h. The obtained surface modified powders were collected by centrifugation, washed at least three times with distilled water and dried at room temperature.

## 2.3 Material characterization

The crystalline phase of the samples was determined by powder XRD with a ULTIMA III diffractometer (Rigaku) using  $\text{CuK}\alpha$  radiation. Morphology of the obtained powders was investigated by scanning electron microscope (S-4200, Hitachi). The size distribution of PEG-*b*-PAAc modified powders in distilled water was measured by dynamic light scattering (DLS) using a Dynamic Light Scattering Particle Size Analyzer LB-550 by Horiba. For FT-IR spectroscopy, samples were mixed with KBr and spectra of the powders were recorded under vacuum conditions using a JASCO FT/IR-6500 spectrometer. Upconversion emission spectra were recorded at room temperature using a RF-5000 Spectrofluorometer by

Shimadzu-Seisakusho under excitation by an IR diode laser at 980 nm. For near infrared emission samples were excited at room temperature with the aid of a Laser Diode by Kamamatsu Photonics K. K. (L9418-04,  $\lambda_p = 977.7 \text{ nm}$ ) using a Thorlabs Laser Diode Controller 2A (LDC 220), Temperature Controller (TED 200) and Laser Diode Mount (6 mm/9 mm). Near infrared emission was detected with a detection system Avantes (AvaSpec-NIR 256-1.7, NIRA, set for 969–1750 nm, Slit-50). In order to investigate chemical durability under acidic conditions bare and PEG-*b*-PAAc modified nanostructures were added into an aqueous HCl solution with an initial pH of 3.0 ( $c(\text{Gd}_2\text{O}_3) = 0.2 \text{ mg/mL}$ ). Under rigorous stirring, the time-dependent change of pH was recorded by use of an Auto Titrator Com-1600 (Hiramura). The zeta-potential of bare and PEG-*b*-PAAc modified nanostructures was determined with a DelsaTM Nano Submicron Particle Size and Zeta Potential analyzer by Beckman Coulter using the disposable cell for zeta-potential unit. Therefore, nanostructures were suspended (0.67 mg/mL) in distilled water ( $\text{pH} = 5.2$ ) or in an aqueous solution of NaOH with an adjusted pH value of 7.3 (corresponding to the pH value of cell culture medium). The zeta-potential was calculated from the mobility by the equipment's software using the Smoluchowski model.

## 2.4 Cytotoxicity tests

B-cell hybridomas (cell line: 83-12-5, purchased by ATCC, CRL-1971) and macrophages (cell line: J774, purchased by ATCC, TIB-67) were used to evaluate cytotoxicity of the obtained nanostructures using in vitro experimental protocols. B-cell hybridomas and macrophages were cultured in RPMI 1640 medium (Sigma-Aldrich) containing 10 % FCS, 2-mercaptoethanol (2ME), 2 mM L-glutamine, penicillin/streptomycin, 0.1 mM HEPES, 0.1 mmol/L non-essential amino acid and 1 mmol/L pyruvic acid for 24 or 48 h with respective nanostructures. Before incubation, the nanostructures were sterilized by use of 70 % ethanol and afterwards the nanostructure culture medium mixture was sonicated for 5 min. Concentrations of the nanostructures in the cell culture media varied between 1 and 500  $\mu\text{g/mL}$ . Viability of B-cell hybridomas and macrophages was analyzed with trypan blue dye-exclusion assay by counting cells in a hemocytometer.

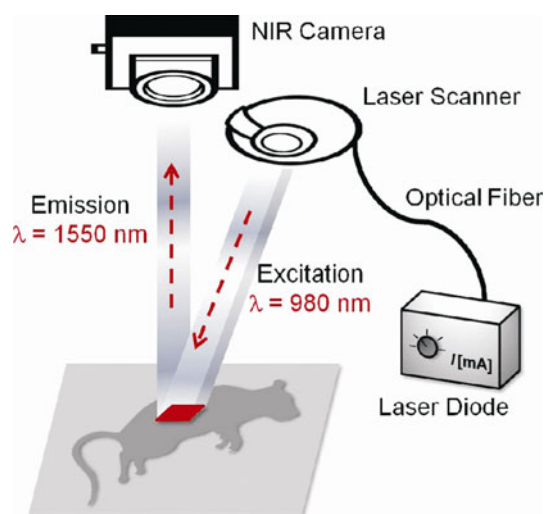
As positive control the anti-cancer drug carboplatin ( $c = 100 \mu\text{g/mL}$ , provided by Nihonkayayaku) was used, which is known to induce cell death [39]. Incubation in cell culture medium without nanostructures demonstrated the negative control simulating cell behavior under ideal conditions. All data obtained for incubated nanostructures were compared to the untreated control.

## 2.5 Staining and fixation of macrophages for in vitro CLSM investigations

In order to stain the cytoplasm of macrophages, macrophages were incubated for 10 min with 1  $\mu\text{M}$  of Cell-Tracker Orange 5-(((4-chloromethyl)benzoyl)amino) tetramethylrhodamine (CMRA) (invitrogen) according to the manufacturer's instructions. CMRA labelled macrophages were then incubated for 12 h with 500  $\mu\text{g}/\text{mL}$   $\text{Gd}_2\text{O}_3:\text{Er}^{3+}, \text{Yb}^{3+}$ . The incubated cells were fixed with 4 % PFA, permeabilized with 0.1 % Triton-X-100 and the nucleus was stained with DAPI (1  $\mu\text{g}/\text{mL}$ ). CMRA and DAPI stained macrophages were enclosed between glass slides for further microscopy analysis. The applied analysis combined CLSM with the measurement of the multi-photon-absorption-induced luminescence from the used nanoparticles according to Farrer et al. [40]. The analysis was carried out using an Axiovert 200 M microscope including a 510 NLO Meta device (Zeiss, Jena, Germany) with helium-neon and femtosecond Ti-sapphire laser (Chameleon, Coherent, Santa Clara, CA). For DAPI detection a two photon excitation with 760 nm tuned Chameleon laser was used. The CMRA was excited at 543 nm using helium–neon laser. For nanoparticle or nanorod detection the chameleon laser was tuned at 980 nm to excite erbium and ytterbium ions. The laser pulse had a repetition rate at 80 MHz and the emission was collected with a 40 $\times$  oil-immersion objective and a bandpass filter with a transmission window from 500 to 550 nm for the green signal (550 nm) or a bandpass filter from 650 to 710 nm for the red luminescence (670 nm). All pictures were taken within the inner section of the cells and the software LSM Image Examiner was used for further analysis.

## 2.6 In vivo distribution in mice organs

In order to study the in vivo distribution of the nanostructures, the mice were injected with 500  $\mu\text{L}$  of  $\text{Gd}_2\text{O}_3:\text{Er}^{3+}, \text{Yb}^{3+}$  nanoparticles or nanorods in HEPES buffer (20 mM, pH = 7.4, 150 mM NaCl) through the tail vein [nanostructure concentration at the injection point at the tail vein:  $c(\text{Gd}_2\text{O}_3:\text{Er}^{3+}, \text{Yb}^{3+}) = 5 \text{ mg}/\text{mL}$ , 2.5 mg per mouse]. Day-0-mice were killed a few hours after injection. Day-1-mice were killed 24 h after injection. After removing the hair of the mice by using commercial depilatory, mice were observed in the “1000-nm NIR in vivo fluorescence bioimaging” (OTN-NIR-IFBI) system NIS-Opt by Shimadzu equipped with a 980-nm laser diode (S4LFT0101/126 SILL155129), a scanner for the fluorescence excitation and an InGaAs-CCD (Xenics Detector), which can detect the image in between 800 and 1,700 nm (Scheme 1). Uniformity of the laser intensity is achieved



**Scheme 1** Schematic representation of the “1000-nm NIR in vivo fluorescence bioimaging” (OTN-NIR-IFBI) system NIS-Opt

by using a scanning galvanometer mirror system that allows scanning the whole mouse body (centimeter range). Near-focus was chosen for the incident laser beam on the animal in order to avoid burning of the biological tissue. The laser power was set to be 4.5 W with a  $\Psi$ Amaki LD Driver & Temperature Controller.

For histological analysis in fluorescence microscope (IX71 by Olympus, equipped with a near infrared source TCLDM9 by Thorlabs), organ samples (liver, spleen, lung, kidneys) were fixed with 10 % formalin and histological evaluation was performed using hematoxylin and eosin (H&E) staining. Urine from day-0 and day-1-mice injected with 85 and 160 nm particles could be collected while sacrificing and was also investigated in fluorescence microscope for residual nanostructures. NIR emission intensity was quantified (integrated density) by greyscale analysis of the obtained fluorescence micrographs using the software ImageJ. Experiments were done under the detection systems' pixel saturation limit (further information and discussion on the lower detection limit and pixel saturation of the used NIR camera systems are provided in Supporting information).

## 3 Results and discussion

### 3.1 Material synthesis and characterization

#### 3.1.1 Phase and morphology

Hydrothermal treatment (HT) and HP methods such as surfactant-free HP, CTAB-assisted HP as well as CTAB- and PEG-6.000-assisted HP were used for the synthesis of various  $\text{Ln}^{3+}$ -doped gadolinium based nanostructures.

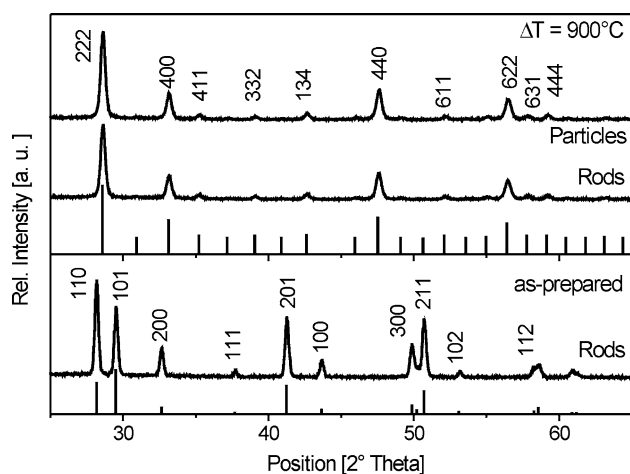


**Fig. 1** X-ray diffraction patterns recorded on as-prepared and annealed ( $T = 900\text{ }^{\circ}\text{C}$ ,  $t = 30\text{ min}$ ) nanorods by HT and particles by CTAB-assisted HP. Reference files:  $\text{Gd}(\text{OH})_3$  [83-2037],  $\text{Gd}_2\text{O}_3$  [12-0797]

X-ray diffraction patterns recorded on samples obtained by HT and CTAB-assisted HP are shown in Fig. 1. Patterns recorded on powders obtained by surfactant-free or CTAB- and PEG-6.000-assisted HP are similar to the pattern for CTAB-assisted HP. As-prepared powders by HT consist of crystalline gadolinium hydroxide ( $\text{Gd}(\text{OH})_3$ ). The powders can be transformed into crystalline gadolinium oxide ( $\text{Gd}_2\text{O}_3$ ) by post-thermal treatment. High annealing temperatures of  $900\text{ }^{\circ}\text{C}$  were chosen in order to remove residual water, hydroxyl or carboxylic groups that may quench photoluminescence of the  $\text{Gd}_2\text{O}_3:\text{Er}^{3+}, \text{Yb}^{3+}$  nanostructures. As-prepared powders obtained by HP are amorphous, but are also transformed into crystalline  $\text{Gd}_2\text{O}_3$  by post-thermal treatment.

The microstructure of the  $\text{Gd}_2\text{O}_3:\text{Er}^{3+}, \text{Yb}^{3+}$  nanostructures was investigated by SEM. As shown in Fig. 2, HP results in spherical shape. Spheres with a diameter of an average value of  $210\text{ nm}$  are obtained by surfactant free HP (Fig. 2a). Matijevic and Hsu [41] originally described the formation of  $\text{Gd}_2\text{O}_3$  particles by HP. However, morphology control is difficult and larger spheres up to  $300\text{ nm}$  in diameter or agglomerates have been observed and are described in literature [42]. Morphology and size can be controlled by the addition of surfactants. Particles with a diameter of an average value of  $160\text{ nm}$  are obtained by addition of CTAB during HP (Fig. 2b). An average particle size of  $85\text{ nm}$  is obtained by addition of a mixture of CTAB and PEG-6.000 (Fig. 2c). Morphology control by cationic surfactant, such as CTAB, is well known and has been described for various lanthanide containing nanostructures [43–45]. Nanostructures obtained by hydrothermal method exhibit rod like structure with lengths of an average value of  $260\text{ nm}$  and diameters of an average value

of  $55\text{ nm}$  resulting in an average aspect ratio of 5 (Fig. 2d). As seen by XRD analysis, HT results in the formation of crystalline gadolinium hydroxide.  $\text{Gd}(\text{OH})_3$  crystallizes in the hexagonal lattice. Hence, anisotropic growth is favored and no templates are required to obtain elongated structures such as nanorods [46–49].

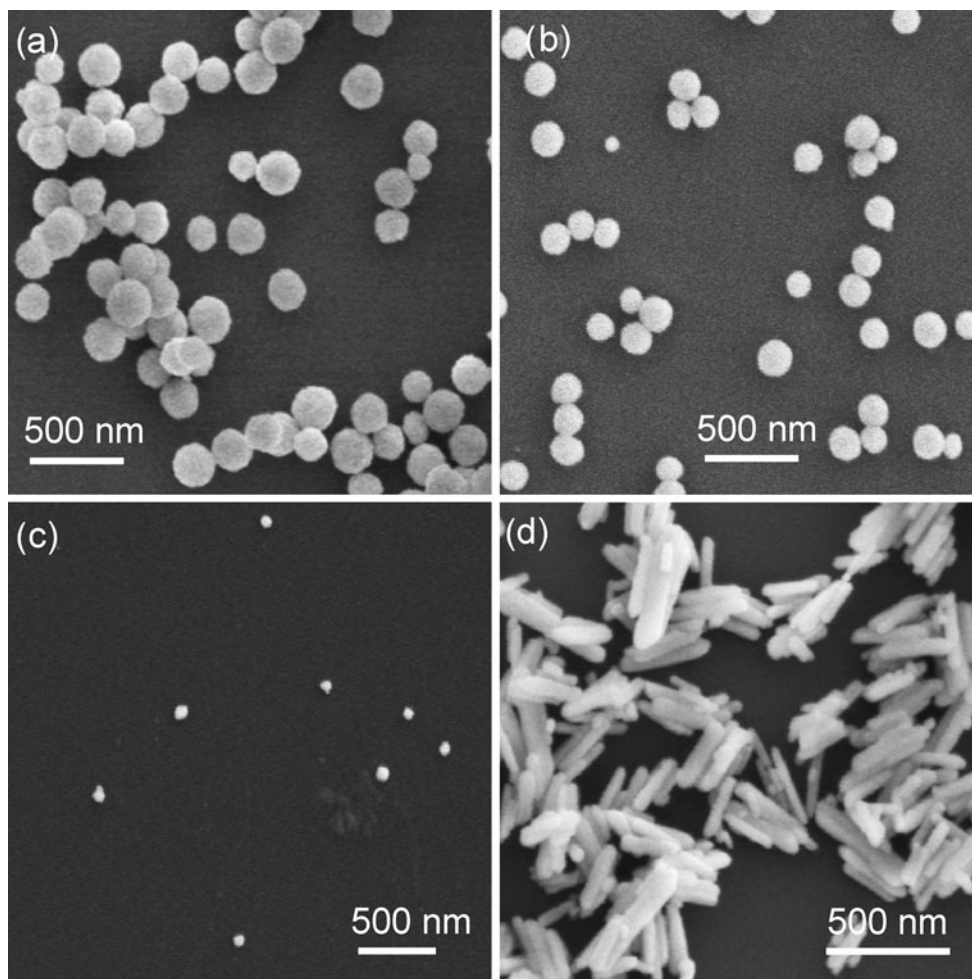
### 3.1.2 Upconversion and NIR emission

Figure 3 shows the upconversion and NIR emission spectra for particles obtained by CTAB-assisted HP (diameter:  $160\text{ nm}$ ) under excitation with  $980\text{-nm}$  wavelength.  $\text{Gd}_2\text{O}_3:\text{Er}^{3+}, \text{Yb}^{3+}$  nanostructures emit green ( $550\text{ nm}$ ) and red ( $670\text{ nm}$ ) luminescence (upconversion emission) as well as NIR light in the range of  $1.5\text{ }\mu\text{m}$  [38]. Particles of  $85$  and  $210\text{ nm}$  as well as rods show similar spectra with emission peaks at the same wavelength range.

### 3.2 Surface modification

Surface modification was effected under aqueous conditions with PEG-*b*-PAAc concentrations of either  $0.6\text{ mg/mL}$  ( $\text{Gd}_2\text{O}_3:\text{Er}^{3+}, \text{Yb}^{3+}:\text{PEG-}b\text{-PAAc} = 1:1$ ) or  $1.2\text{ mg/mL}$  ( $\text{Gd}_2\text{O}_3:\text{Er}^{3+}, \text{Yb}^{3+}:\text{PEG-}b\text{-PAAc} = 1:2$ ). Prior to the addition of  $0.6\text{ mg/mL}$  PEG-*b*-PAAc, PEG-6.000 was added to the aqueous nanostructure dispersion in order to increase its viscosity and hereby hinder the formation of large agglomerates. Due to the positive surface charge of  $\text{Gd}_2\text{O}_3$ , confirmed by  $\zeta$ -potential measurements, the polyacrylic acid group (PAAc) of the co-block polymer can be electrostatically adsorbed on the nanostructure surface. The PEG-*b*-PAAc modification of the  $\text{Gd}_2\text{O}_3:\text{Er}^{3+}, \text{Yb}^{3+}$  nanostructures was confirmed by FT-IR spectra as shown in Fig. 4.

Spectra of annealed, bare nanostructures show peaks for metal-oxygen bonds in the range of  $500\text{ cm}^{-1}$ , which confirms the formation of gadolinium oxide phase by post-thermal treatment. The presence of C=O and C–O–C bands can be assigned to impurities, such as residual carbonates resulting from an incomplete decomposition of the original precipitated  $\text{Gd}(\text{OH})\text{CO}_3 \cdot \text{H}_2\text{O}$  particles to  $\text{Gd}_2\text{O}_3$ ,  $\text{H}_2\text{O}$  and  $\text{CO}_2$  [41]. Those carbonates are extremely difficult to remove and could also be found in analogous yttria nanoparticles annealed at  $900\text{ }^{\circ}\text{C}$  [50]. Further,  $\text{CO}_2$  from the atmosphere can absorb on the particle surface due to the basic character of  $\text{Gd}_2\text{O}_3$  [22]. After surface modification peaks appear at  $2900$ ,  $1500$  and  $1100\text{ cm}^{-1}$ . Those are referred to C–H bonds, C=O bonds in PAAc and C–O–C bond in PEG. Higher PEG-*b*-PAAc concentration results in higher intensity of those peaks. However, we suggest that lower concentration is sufficient for a successful surface modification. The broad band in the range  $3,500\text{ cm}^{-1}$  is



**Fig. 2** Scanning electron micrographs of  $\text{Gd}_2\text{O}_3:\text{Er}^{3+}\text{Yb}^{3+}$  nanostructures obtained by **a** surfactant-free ( $\langle d_{\text{SEM}} \rangle = 209 \pm 28$  nm), **b** CTAB-assisted ( $\langle d_{\text{SEM}} \rangle = 158 \pm 23$  nm) and **c** CTAB- and PEG-

6,000-assisted HP ( $\langle d_{\text{SEM}} \rangle = 86 \pm 12$  nm) as well as **d** HT ( $\langle d_{\text{SEM}} \rangle = 53 \pm 18$  nm,  $\langle l_{\text{SEM}} \rangle = 262 \pm 91$  nm,  $\langle l/d_{\text{SEM}} \rangle = 5 \pm 1.6$ )

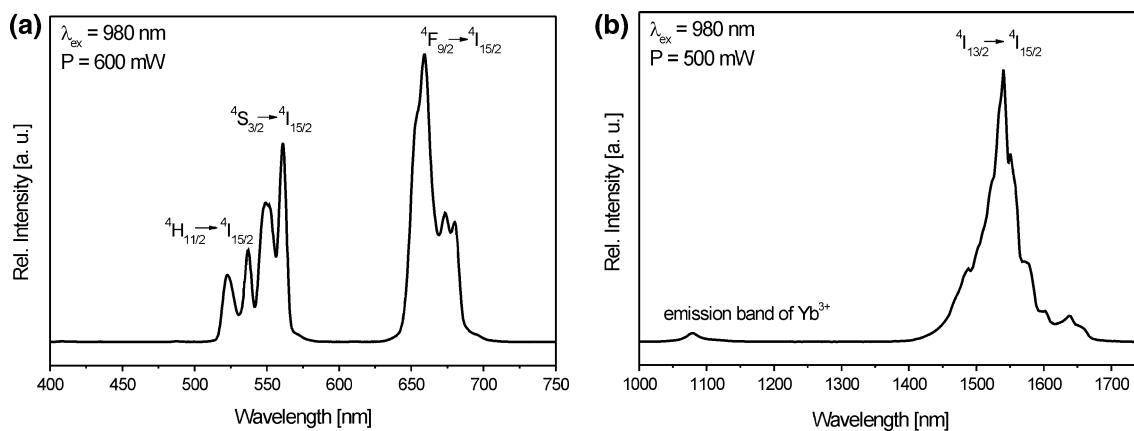


**Fig. 3** **a** Upconversion and **b** NIR emission spectra recorded on  $\text{Gd}_2\text{O}_3:\text{Er}^{3+}, \text{Yb}^{3+}$  particles obtained by CTAB-assisted HP ( $P$  laser power at the source point)

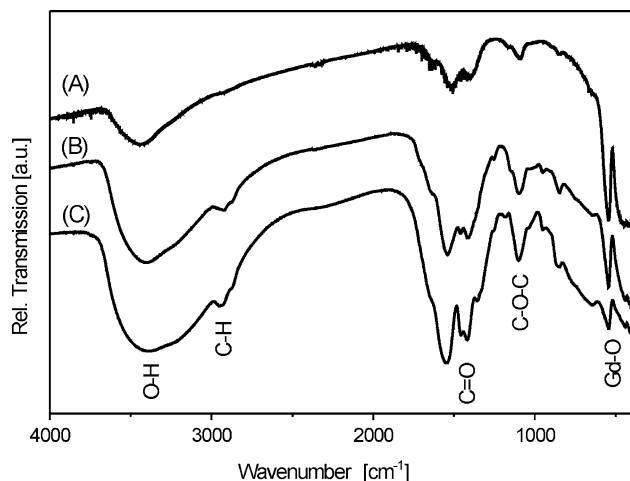


**Fig. 4** FT-IR spectra of bare (A) and PEG-*b*-PAAc modified (B: c(PEG-*b*-PAAc) = 0.6 mg/mL, PEG-6.000 assisted; C: c(PEG-*b*-PAAc) = 1.2 mg/mL) Gd<sub>2</sub>O<sub>3</sub>:Er<sup>3+</sup>,Yb<sup>3+</sup> nanostructures obtained by CTAB-assisted HP (analogous spectra were recorded on all other samples)

assigned to O–H groups originating from surface modification in aqueous medium.

### 3.2.1 Dynamic light scattering

The size distributions of PEG-*b*-PAAc modified nanostructures dispersed in water are displayed in Fig. 5 suggesting that the modified nanoparticles are well dispersed in aqueous solutions. The hydrodynamic mean diameters are 260, 190 and 90 nm for particles obtained by HP, by CTAB-assisted HP and CTAB- and PEG-6.000-assisted HP. Those values are in good agreement with particle sizes observed in SEM (210, 160 and 85 nm). In case of nanorods (SEM: 260 × 55 nm)

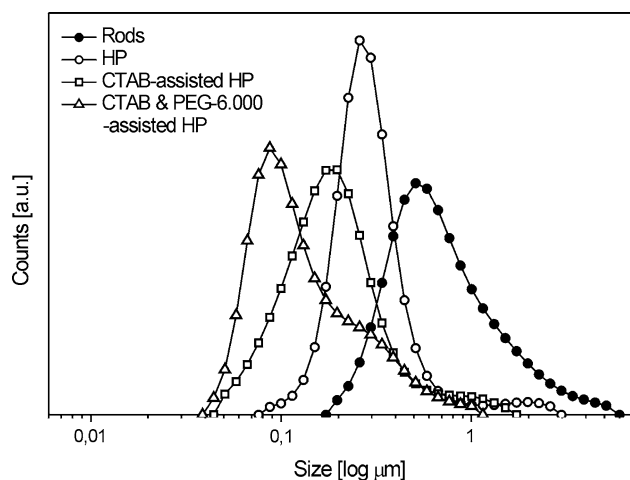
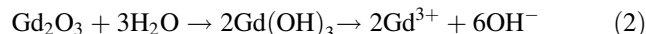


**Fig. 5** Hydrodynamic diameter distribution of the PEG-*b*-PAAc modified Gd<sub>2</sub>O<sub>3</sub>:Er<sup>3+</sup>,Yb<sup>3+</sup> nanostructures obtained by surfactant-free (open circle), CTAB-assisted (open square), CTAB- and PEG-6.000-assisted HP (open triangle) and HT (filled circle)

the measured hydrodynamic mean diameter is 500 nm indicating a tendency to form agglomerations. It must also be mentioned that DLS is a standard technique for the investigation of spherical structures, while in case of rod-like structures the assumption that all particles are spherical is not valid and their analysis is much more complex. Due to Brownian motion particles move randomly, whereas elongated structures move rapidly in the elongated direction, but slowly in the other direction. During the DLS measurement an average over those rapid and slow movements of the rods over time is recorded and an equivalent sphere is calculated [51, 52]. Therefore, the hydrodynamic size can differ significantly from the true size of the structures as observed in SEM.

### 3.2.2 Chemical durability

Under acidic conditions, as found, e.g. inside macrophages, lanthanide oxides, Ln<sub>2</sub>O<sub>3</sub>, suffer from a poor chemical durability [53] resulting in their dissolution and formation of free lanthanide ions. The chemical durability of the obtained Gd<sub>2</sub>O<sub>3</sub>:Er<sup>3+</sup>,Yb<sup>3+</sup> nanostructures was investigated by adjusting the pH of an aqueous nanostructure dispersion to 3.0 with HCl. The change in pH was recorded as a function of time. Generally, in the presence of HCl, metal oxides react to metal chloride and water (Eq. 1). GdCl<sub>3</sub> is soluble in water leading to the formation of Gd<sup>3+</sup> and Cl<sup>-</sup> ions. During this reaction H<sup>+</sup> ions are consumed and consequently the reaction is accompanied by an increase in pH of the reaction medium. Further, most lanthanide oxides react spontaneously with water to lanthanide hydroxides (Eq. 2) [54]. The partial dissociation of Gd(OH)<sub>3</sub> in aqueous media results in the formation of Gd<sup>3+</sup> as well as OH<sup>-</sup> ions leading to an increase in pH (pK<sub>a</sub>(Gd(OH)<sub>3</sub>) = 9.4, pK<sub>b</sub>(Gd(OH)<sub>3</sub>) = 5.7). Therefore, the chemical durability of the nanostructures can be evaluated based on the change in pH of the solution, whereas an increase in pH of the nanostructure suspension indicates the partial dissolution of Gd<sub>2</sub>O<sub>3</sub>.



As obvious from Fig. 6, the immediate increase of the pH from initial 3.0 to a saturation value of 6.4 confirms the poor chemical durability of bare Gd<sub>2</sub>O<sub>3</sub> nanostructures. On the other hand, after modification with PEG-*b*-PAAc particles and rods show good chemical durability.

### 3.3 In vitro cytotoxicity

In our previous work, the in vitro cytotoxicity of Gd<sub>2</sub>O<sub>3</sub>:Er<sup>3+</sup>,Yb<sup>3+</sup> nanostructures towards B-cell hybridomas and macrophages was investigated by a set of cytotoxicity assays [38, 55]. Briefly, we found no cytotoxic

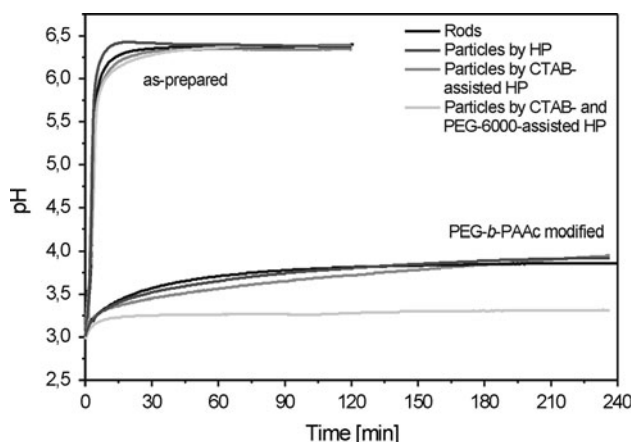


**Fig. 6** Chemical durability of bare and PEG-*b*-PAAc modified  $\text{Gd}_2\text{O}_3:\text{Er}^{3+}, \text{Yb}^{3+}$  nanostructures

effect after incubation of up to 500  $\mu\text{g}/\text{mL}$   $\text{Gd}_2\text{O}_3:\text{Er}^{3+}, \text{Yb}^{3+}$  with B-cells hybridomas, but low viabilities have been observed in case of macrophages (Fig. 7a). The cytotoxic effect is deduced to the uptake of the nanostructures by macrophages, followed by a partial dissolution and release of toxic  $\text{Gd}^{3+}$  ions due to the poor chemical durability of gadolinium oxide under acidic conditions inside macrophages. Surface modification with PEG-*b*-PAAc improves the chemical durability of the nanostructures, resulting in viabilities of macrophages that are at least 20–40 % higher than the viabilities of cell cultures incubated with bare nanostructures (Fig. 7b, c).

Besides the improved chemical durability of modified  $\text{Gd}_2\text{O}_3:\text{Er}^{3+}, \text{Yb}^{3+}$ , changes in the surface properties have been suggested as a potential reason for the observed biocompatibility after PEG-*b*-PAAc modification. It is known that the interaction between cells and nanostructured

materials depends not only on size and morphology but also on surface charge [56]. Due to the generally negatively charged cell membrane, nanostructures with a positive surface charge should be uptaken more easily than those with a negative surface charge. Measurement of the  $\zeta$ -potential of bare and PEG-*b*-PAAc modified nanostructures revealed a positive surface charge before, a negative surface charge after modification. Consequently, a higher incorporation rate, and therefore lower viability, is expected for bare nanostructures when compared to modified  $\text{Gd}_2\text{O}_3:\text{Er}^{3+}, \text{Yb}^{3+}$ . For verification, bare and PEG-*b*-PAAc modified  $\text{Gd}_2\text{O}_3:\text{Er}^{3+}, \text{Yb}^{3+}$  nanorods and nanoparticles (CTAB-assisted HP,  $d \sim 160$  nm) have been incubated with macrophages, followed by investigation in CLSM.

### 3.4 In vitro cellular uptake (CLSM)

In order to monitor the in vitro cellular uptake of  $\text{Gd}_2\text{O}_3:\text{Er}^{3+}, \text{Yb}^{3+}$  nanostructures by macrophages as a function of surface modification, we used CLSM. Bare and PEG-*b*-PAAc modified nanorods and particles (160 nm) were incubated with macrophages for 12 h, followed by fixation of the cells. Cytoplasm was stained with Cell-Tracker Orange (CMRA), which emits in orange range (576 nm) under 543-nm excitation. Blue (461 nm,  $\lambda_{\text{ex}} = 760$  nm) emitting DAPI was used to stain the nucleus. Under 980-nm excitation green (550 nm) and red (670 nm) upconversion emission from  $\text{Gd}_2\text{O}_3:\text{Er}^{3+}, \text{Yb}^{3+}$  can be detected in CLSM allowing the localization of the nanostructures (Fig. 8).

In case of bare nanoparticles obtained by CTAB-assisted HP (Fig. 8a), red and green upconversion emission was detected in cytoplasm confirming the uptake of

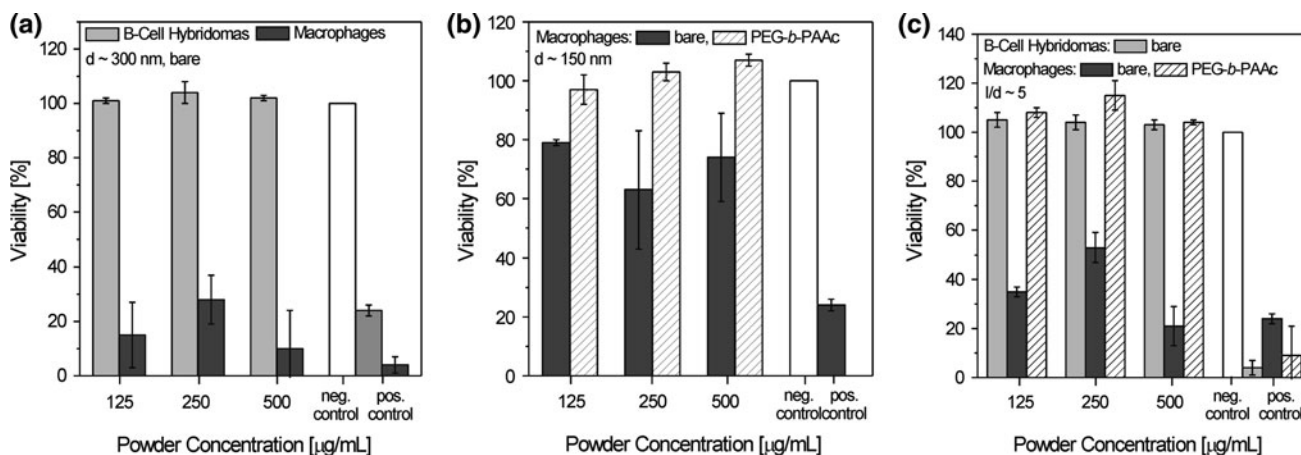


**Fig. 7** In vitro cytotoxicity determined by trypan blue assay. **a** Viability of B-cell hybridomas (incubation time 48 h) and macrophages (incubation time 24 h) after incubation with bare particles obtained by homogeneous precipitation. **b** Viability of macrophages incubated with bare and PEG-*b*-PAAc modified

particles obtained by surfactant assisted HP (incubation time 24 h). **c** Viability of bare and PEG-*b*-PAAc modified nanorods incubated with B-cell hybridomas and macrophages (incubation time 24 h). Negative control: medium alone. Positive control: carboplatin



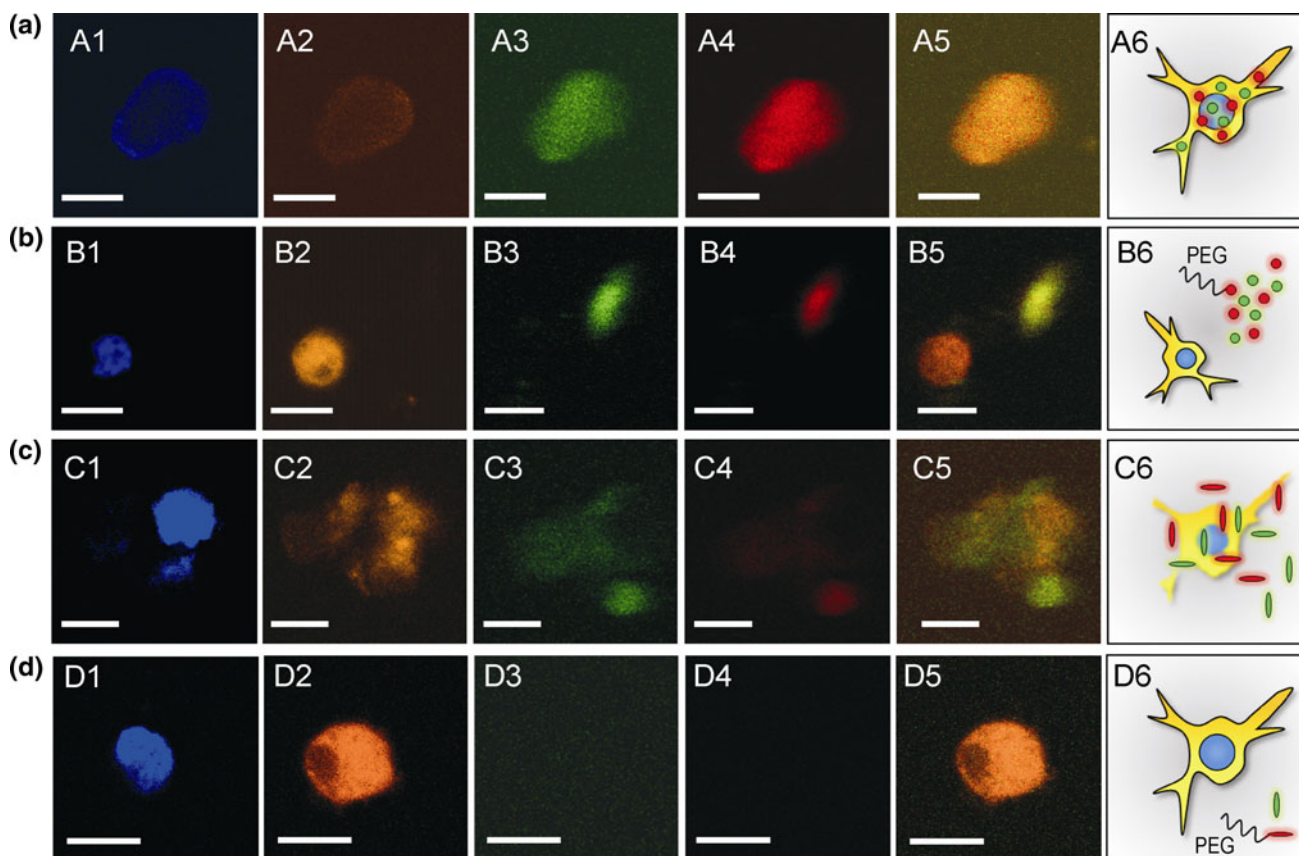


**Fig. 8** CLSM images of macrophages incubated with **a** bare and **b** PEG-*b*-PAAc modified particles as well as **c** bare and **d** PEG-*b*-PAAc modified rods. Scale bar 10  $\mu\text{m}$ . 1 DAPI stained nucleus ( $\lambda_{\text{ex}} = 760 \text{ nm}$ ,  $\lambda_{\text{em}} = 461 \text{ nm}$ ). 2

( $\lambda_{\text{ex}} = 543 \text{ nm}$ ,  $\lambda_{\text{em}} = 576 \text{ nm}$ ). 3 Green (550 nm) and 4 red (670 nm) upconversion emission of  $\text{Gd}_2\text{O}_3:\text{Er}^{3+}, \text{Yb}^{3+}$  under 980-nm excitation. 5 Overlay. 6 Schematic representation

$\text{Gd}_2\text{O}_3:\text{Er}^{3+}, \text{Yb}^{3+}$  by the macrophage. After modification with PEG-*b*-PAAc (Fig. 8b) no upconversion signal is detected in the cytoplasm but next to macrophage. This observation indicates that PEG-*b*-PAAc modified particles have not been taken up by the cell. Further, the observation of healthy macrophages is in agreement with the high viability of macrophages incubated with modified nanostructures determined by trypan blue assay (Fig. 7b). As obvious from Fig. 8c, green and red luminescence emitted from bare nanorods can be detected in and around cytoplasm of the presented dead macrophage revealing the cytotoxic effect (Fig. 7c) and cellular uptake of bare  $\text{Gd}_2\text{O}_3:\text{Er}^{3+}, \text{Yb}^{3+}$  nanorods. Macrophages incubated with PEG-*b*-PAAc modified nanorods are in healthy configuration. Only weak green upconversion emission could be detected outside cytoplasm (Fig. 8d). These results confirm the cellular uptake of bare  $\text{Gd}_2\text{O}_3:\text{Er}^{3+}, \text{Yb}^{3+}$ . On the other hand, less nanostructures with PEG-*b*-PAAc modification have been uptaken by macrophages. This is in agreement with the reduction of non-specific uptake by macrophages reported for PEG-modified nanostructures, such as iron oxide or poly(lactic acid) (PLA) nanoparticles [57–59].

The results obtained from in vitro cytotoxicity assays and observations made in CLSM show that the introduction of a PEG-*b*-PAAc shell on the gadolinium oxide core structure provides good biocompatibility under studied conditions. This fact can be assigned first to an improved chemical durability under acid conditions and second to a PEG-*b*-PAAc-induced decrease in cellular uptake.

### 3.5 In vivo distribution of PEG-*b*-PAAc modified $\text{Gd}_2\text{O}_3:\text{Er}^{3+}, \text{Yb}^{3+}$

The in vivo distribution of PEG-*b*-PAAc modified  $\text{Gd}_2\text{O}_3:\text{Er}^{3+}, \text{Yb}^{3+}$  nanostructures was investigated by using C57BL/6 mice. Nanostructures were suspended in HEPES buffer at 500  $\mu\text{g}/\text{mL}$  concentration and were injected through tail vein (2.5 mg  $\text{Gd}_2\text{O}_3:\text{Er}^{3+}, \text{Yb}^{3+}$  per mouse). After a few hours (day-0-mice), respectively 24 h (day-1-mice) mice have been killed and nanostructure distribution was observed in the OTN-NIR-FIB system NIS-Opt. Figure 9 shows the NIR emission intensity under 980-nm excitation on day 0 and day 1. Mice treated with particles of 210 and 160 nm diameter show intensive

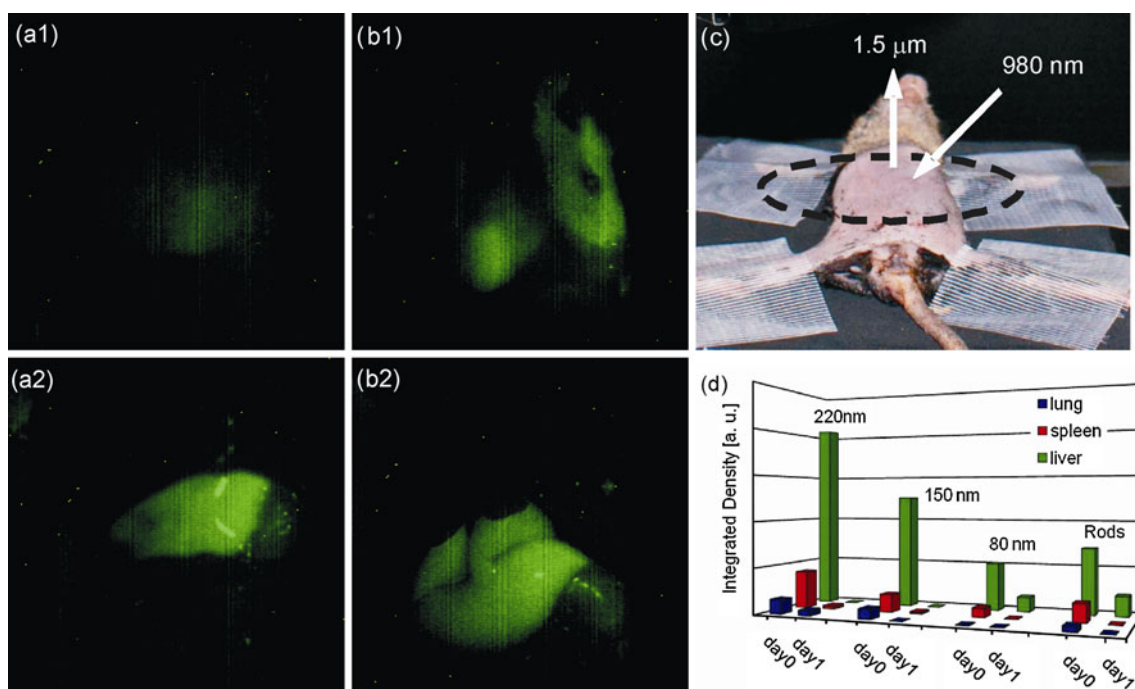


**Fig. 9** OTN-NIR-IFBI false-color images of mice treated with PEG-*b*-PAAc modified  $\text{Gd}_2\text{O}_3:\text{Er}^{3+}, \text{Yb}^{3+}$  nanoparticles of **a** 210 nm and **b** 160 nm in diameter (*l* whole body, 2 opened body, day-0-mouse).

signals on day 0 through the mice's skin (a1 and b1). The signal is originating from  $\text{Gd}_2\text{O}_3:\text{Er}^{3+}, \text{Yb}^{3+}$  particles accumulated in the liver as confirmed by observation of the dissected mice (a2 and b2). In case of smaller particles and nanorods, no signal was detected from the whole body, but the accumulation of nanostructures was confirmed by investigating single organs (Fig. 9d) as well as histological sections of liver, lung, spleen and kidneys (Fig. 10).

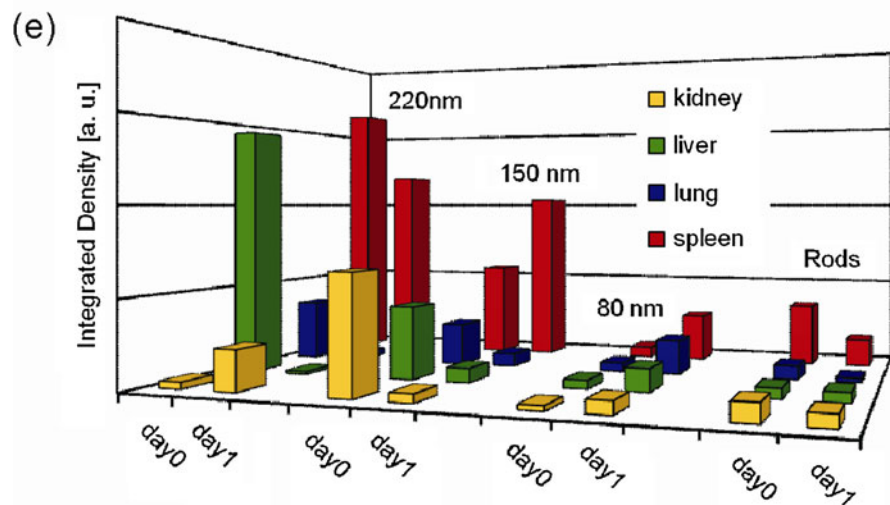
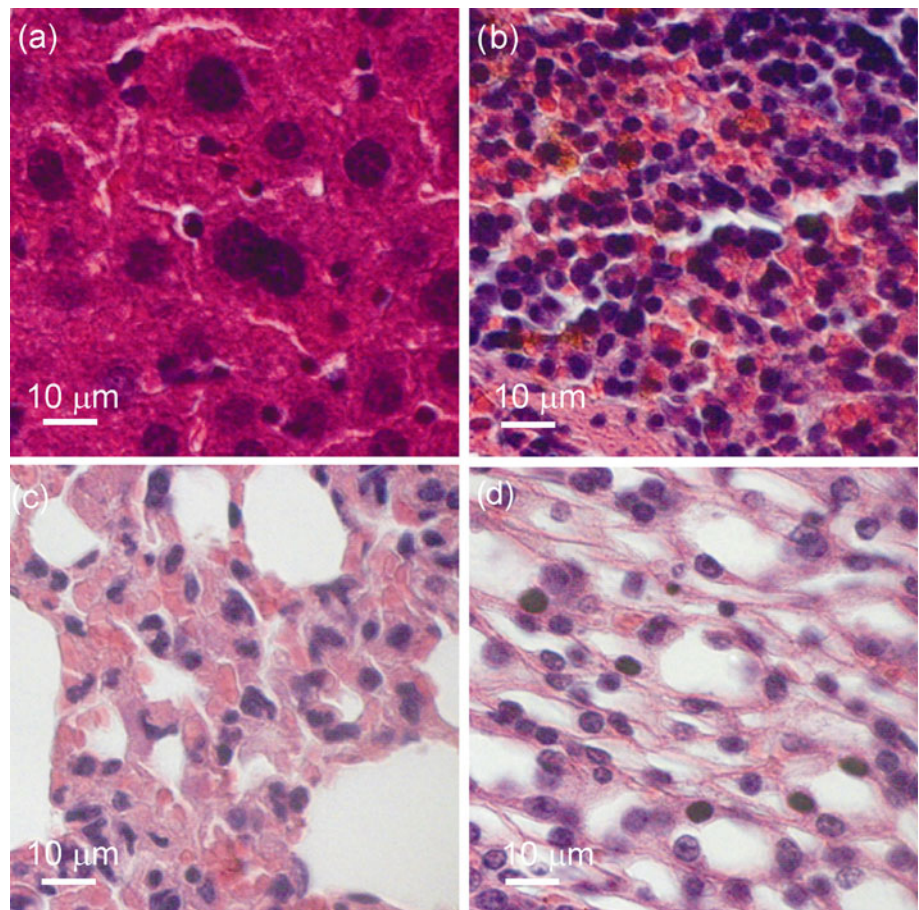
The organ biodistribution study on day 0 reveals that the nanostructures were mainly distributed in liver, spleen and lung. Herein, signal intensity decreased with decreasing particle diameter from 210 to 85 nm. The emission intensity in case of nanorods is in between those intensities measured for 85 and 160 nm particles (Fig. 9d). NIR–NIR upconversion emission signals from organs of day-1-mice reveal a strong decrease in signal intensity suggesting the clearance of the nanostructures throughout the time course of this study. Fluorescence microscopic analysis of histological sections taken from liver, spleen, lung and kidney reveals a similar trend (Fig. 10e). Strongest NIR emission is detected from spleen and liver, whereas the signal intensity decreases from largest particles (210 nm, surfactant-free HP) to nanorods and smallest particles (85 nm, CTAB- and PEG-6.000-assisted HP).

The uptake of nanostructures by clearance organs (liver and spleen) and lung has been reported for various nanoprobe for biomedical applications [60–62]. Gratton et al. [63] investigated the uptake and elimination

**c** Investigated body part. **d** NIR emission intensity (integrated density) from lung, liver and spleen of day-0- and day-1-mice.  $P_{\text{Laser}} = 4.5 \text{ W}$ ,  $\lambda_{\text{ex}} = 980 \text{ nm}$ ,  $\lambda_{\text{em}} = 1.5 \mu\text{m}$

of  $^{64}\text{Cu}$ -labeled DOTA-nanoparticles by time-resolved MicroPET imaging. According to the authors, the accumulation in clearance organs and the short elimination time after injection indicates the quick recognition of nanostructures as foreign followed by the removal from systemic circulation by the reticuloendothelial system (RES). Herein, Kupffer cells play a central role as shown by Danscher et al. [64]. The authors reported the uptake of 2 and 40 nm gold nanoparticles primarily by Kupffer cells in the liver and secondarily by macrophages in the spleen. Kryza et al. [65] reported the free circulation of less than 5 nm in diameter  $\text{Gd}_2\text{O}_3$  nanoparticles with a polysiloxane shell in the blood without RES uptake, and observed renal elimination of the nanostructures by SPECT, MR and optical imaging. Silicon quantum dots are reported to accumulate in the urinary bladder as well as the liver and are excreted via renal filtration shortly after injection, whereas the main site for accumulation of remaining quantum dots 48 h after injection is the liver [66]. In our study, fluorescence microscopic analysis of urine samples taken from day-0- and day-1-mice injected with 85 and 160 nm particles showed a low content of green and NIR upconverting  $\text{Gd}_2\text{O}_3:\text{Er}^{3+}, \text{Yb}^{3+}$  particles of 160 nm in diameter. Further NIR emission was detected from histological sections of the kidneys (Fig. 10e). This observation suggests minor renal elimination of the nanostructures from the body. However, based on obtained OTN-NIR-FIB images and due to nanostructures size [67] from 85 to

**Fig. 10** Histological sections (violet: haematoxylin staining of the nuclei, red: eosin staining of eosinophilic structures such as intracellular or extracellular proteins including cytoplasm and red blood cells) of **a** liver, **b** spleen, **c** lung and **d** kidney of day-0-mice treated with 210 nm particles as well as **e** NIR emission intensity (integrated density) from histological sections of day-0- and day-1-mice's organs ( $P_{\text{Laser}} = 650 \text{ mW}$ ,  $\lambda_{\text{ex}} = 980 \text{ nm}$ ,  $\lambda_{\text{em}} = 1.5 \mu\text{m}$ )



210 nm, uptake by Kupffer cells in the liver and macrophages in the spleen is proposed to be the main clearance mechanism. Hereby it must be taken into account that those results clearly show the existence of  $\text{Gd}_2\text{O}_3:\text{Er}^{3+}, \text{Yb}^{3+}$  nanostructures in lung, liver, spleen and kidney. However, a potential biodistribution in other organs cannot be completely ruled out as the lower detection limit of this newly developed in vivo NIR-based imaging system is still

unclear. The lower limit is still remained to be researched and further investigations including the confirmation of the biodistribution by methods such as ICP-MS are recently underway.

The influence of geometry and surface charge on bio-distribution was studied by Arnida et al. [68]. A reduced uptake of PEGylated gold nanorods by macrophages was compared to PEGylated nanoparticles. Nanoparticles of

negative surface charge accumulated in the liver at notably higher extent than nanorods of almost neutral charge, which was deduced to different morphology and surface charge. We observed reduced NIR emission from organs of mice treated with nanorods, which may be, in accordance to Armida et al., due to a reduced accumulation of rod-like structures in liver, spleen and lung when compared to nanoparticles. As both of our PEG-*b*-PAAc modified  $\text{Gd}_2\text{O}_3:\text{Er}^{3+},\text{Yb}^{3+}$  nanostructures, rods and particles, exhibit a negative surface charge, the influence of morphology may be more important than that of the surface charge and a morphology driven accumulation and blood circulation time cannot be ruled out.

#### 4 Conclusions

Erbium and ytterbium doped gadolinium oxide ( $\text{Gd}_2\text{O}_3:\text{Er}^{3+},\text{Yb}^{3+}$ ) rod-like structures with an aspect ratio of 5 as well as particles of 210, 160 and 85 nm in diameter have been synthesized by hydrothermal and homogeneous precipitation methods. The obtained nanostructures show up-conversion and NIR emission under 980-nm excitation. Bright emission in the NIR range, observed in NIR fluorescence microscope, makes  $\text{Gd}_2\text{O}_3:\text{Er}^{3+},\text{Yb}^{3+}$  promising candidates as biomarkers for the “over 1000-nm NIR in vivo fluorescence bioimaging” system. The cytotoxic behavior of the obtained nanostructures was investigated by incubation with B-cell hybridomas and macrophages. No cytotoxic effect was observed towards B-cell hybridomas. In contrast, viability of macrophages was reduced when incubated with bare nanostructures. This fact was deduced to the release of toxic  $\text{Gd}^{3+}$  ions due to the poor chemical durability of gadolinium oxide under acidic conditions corresponding to the environment inside macrophages. Surface modification with PEG-*b*-PAAc improved the chemical durability and resulted in good biocompatibility towards macrophages up to the highest tested powder concentration (500  $\mu\text{g}/\text{mL}$ ). Further, CLSM revealed a strong influence of the PEG-*b*-PAAc modification on the uptake behavior of nanostructures by macrophages. While bare nanostructures are easily uptaken, tendency for uptake of modified nanostructures is less pronounced. This observation is assigned to the change in surface charge from positive to negative range by introduction of PEG-*b*-PAAc chains on the nanostructure surface. The in vivo distribution of PEG-*b*-PAAc modified nanostructures in mouse organs was investigated in the OTN-NIR-IFBI system, revealing nanostructures in clearance organs (liver, kidneys and spleen) and lung. Most intensive emission was detected from particles larger than 100 nm. Histological sections of the organs confirmed those results. Further, elimination studies in fluorescence

microscope suggest the clearance of the nanostructures via liver and kidneys. The observed biocompatibility and strong UPC as well as NIR emission under 980-nm excitation make those PEG-*b*-PAAc modified  $\text{Gd}_2\text{O}_3:\text{Er}^{3+},\text{Yb}^{3+}$  nanoparticles and rods promising candidates for NIR bioimaging.

**Acknowledgment** This work was partly supported by Matching Fund Subsidy from MEXT (Ministry of Education, Culture, Sports, Science and Technology), 2006–2010 and 2009–2013. The authors thank Dr. Lionel Vayssieres (WPI Center for Materials NanoArchitectonics (MANA), National Institute for Materials Science (NIMS), Tsukuba, Japan) for scientific discussion and provision of the zeta-potential equipment.

#### References

- Hong YL, Fan HS, Li B, Guo B, Liu M, Zhang XD. Fabrication, biological effects, and medical applications of calcium phosphate nanoceramics. *Mater Sci Eng R*. 2010;70:225–42.
- Madurantakam PA, Cost CP, Simpson DG, Bowlin GL. Science of nanofibrous scaffold fabrication: strategies for next generation tissue-engineering scaffolds. *Nanomedicine*. 2009;4:193–206.
- Poinern GEJ, Fawcett D, Ng YJ, Ali N, Brundavanam RK, Jiang ZT. Nanoengineering a biocompatible inorganic scaffold for skin wound healing. *J Biomed Nanotechnol*. 2010;6(Special issue): 497–510.
- Kallinteri P, Higgins S, Hutcheon GA, St Pourcain CB, Garnett MC. Novel functionalized biodegradable polymers for nanoparticle drug delivery systems. *Biomacromolecules*. 2005;6: 1885–94.
- Kreuter J, Shamenkov D, Petrov V, Ränge P, Cychutek K, Koch-Brandt C, Alyautdin R. Apolipoprotein-mediated transport of nanoparticle-bound drugs across the blood-brain barrier. *J Drug Target*. 2002;10:317–25.
- Hughes GA. Nanostructure-mediated drug delivery. *Nanomedicine*. 2005;1:22–30.
- Tosi G, Costantino L, Rivasi F, Ruozi B, Leo E, Vergoni AV, Tacchi R, Bertolini A, Vandelli MA, Forni F. Targeting the central nervous system: in vivo experiments with peptide-derivatized nanoparticles loaded with Loperamide and Rhodamine-123. *J Control Release*. 2007;122:1–9.
- Ravi Kumar MNV. Nano and microparticles as controlled drug delivery devices. *J Pharm Pharm Sci*. 2000;3:234–58.
- Yan E, Fu Y, Wang X, Ding Y, Qian H, Wang CH, Hu Y, Jiang X. Hollow chitosan-silica nanospheres for doxorubicin delivery to cancer cells with enhanced antitumor effect in vivo. *J Mater Chem*. 2011;21:3147–55.
- Rosenblum LT, Kosaka N, Mitsunaga M, Choyke PL, Kobayashi H. In vivo molecular imaging using nanomaterials: general in vivo characteristics of nano-sized reagents and applications for cancer diagnosis (review). *Mol Membr Biol*. 2010;27:274–85.
- Corr SA, Rakovich YP, Gun'ko YK. Multifunctional magnetic-fluorescent nanocomposites for biomedical applications. *Nanoscale Res Lett*. 2008;3:87–104.
- Pautler M, Brenner S. Nanomedicine: promises and challenges for the future of public health. *Int J Nanomed*. 2010;5:803–9.
- Portney NG, Ozkan M. Nano-oncology: drug delivery, imaging, and sensing. *Anal Bioanal Chem*. 2006;384:620–30.
- Kotov NA, Winter JO, Clements IP, Jan E, Timko BP, Campidelli S, Pathak S, Mazzatenta A, Lieber CM, Prato M, Bellamkonda RV, Silva GA, Wong Shi Kam N, Patolsky F, Ballerini

- L. Nanomaterials for neural interfaces. *Adv Mater.* 2009;21:3970–4004.
15. Shaner NC, Lin MZ, McKeown MR, Steinbach PA, Hazelwood KL, Davidson MW, Tsien RY. Improving the photostability of bright monomeric orange and red fluorescent proteins. *Nat Methods.* 2008;5:545–51.
  16. Chudakov DM, Matz MV, Lukyanov S, Lukyanov KA. Fluorescent proteins and their applications in imaging living cells and tissues. *Physiol Rev.* 2010;90:1103–63.
  17. Michalet X, Pinaud FF, Bentolila LA, Tsay JM, Doose S, Li JJ, Sundaresan G, Wu AM, Gambhir SS, Weiss S. *Science.* 2005;307:538–44.
  18. Sharma P, Brown S, Walter G, Santra S, Moudgil B. Nanoparticles for bioimaging. *Adv Colloid Interface Sci.* 2006;123–126:471–85.
  19. Lu Z, Zhu Z, Zheng X, Qiao Y, Guo J, Li CM. Biocompatible fluorescence-enhanced ZrO<sub>2</sub>-CdTe quantum dot nanocomposite for in vitro cell imaging. *Nanotechnology.* 2011;22:155604.
  20. Vela J, Htoon H, Chen Y, Park YS, Ghosh Y, Goodwin PM, Werner JH, Wells NP, Casson JL, Hollingsworth JA. Effect of shell thickness and composition on blinking suppression and the blinking mechanism in ‘giant’ CdSe/CdS nanocrystal quantum dots. *Biophotonics.* 2010;3:706–17.
  21. Frantsuzov PA, Marcus RA. Explanation of quantum dot blinking without the long-lived trap hypothesis. *Phys Rev B.* 2005;72:155321.
  22. Cotton S. Lanthanide and actinide chemistry. Chichester: Wiley; 2006.
  23. Hanaoka K. Development of responsive lanthanide-based magnetic resonance imaging and luminescent probes for biological applications. *Chem Pharm Bull.* 2010;58:1283–94.
  24. Andraud C, Maury O. Lanthanide complexes for nonlinear optics: from fundamental aspects to applications. *Eur J Inorg Chem.* 2009;29–30:4357–71.
  25. Das GK, Heng BC, Ng SC, White T, Loo JSC, D’Silva L, Padmanabhan P, Bhakoo KK, Selvan ST, Tan TTY. Gadolinium oxide ultranarrow nanorods as multimodal contrast agents for optical and magnetic resonance imaging. *Langmuir.* 2010;26:8959–65.
  26. Pang M, Liu D, Lei Y, Song S, Feng J, Fan W, Zhang H. Rare-earth-doped bifunctional alkaline-earth metal fluoride nanocrystals via a facile microwave-assisted process. *Inorg Chem.* 2011;50:5327–9.
  27. Kamimura M, Miyamoto D, Saito Y, Soga K, Nagasaki Y. Design of poly(ethylene glycol)/streptavidin coimmobilized up-conversion nanophosphors and their application to fluorescence biolabeling. *Langmuir.* 2008;24:8864–70.
  28. Xiong L, Chen Z, Tian Q, Cao T, Xu C, Li F. High contrast upconversion luminescence targeted imaging in vivo using peptide-labeled nanophosphors. *Anal Chem.* 2009;81:8687–94.
  29. Anderson RR, Parrish JA. The optics of human skin. *J Invest Dermatol.* 1981;77:13–9.
  30. Hilderbrand SA, Shao F, Salthouse C, Mahmood U, Weissleder R. Upconverting luminescent nanomaterials: application to in vivo bioimaging. *Chem Commun.* 2009;28:4188–90.
  31. Nyk M, Kumar R, Ohulchanskyy TY, Bergey EJ, Prasad PN. High contrast in vitro and in vivo photoluminescence bioimaging using near infrared to near infrared up-conversion in Tm<sup>3+</sup> and Yb<sup>3+</sup> doped fluoride nanophosphors. *Nano Lett.* 2008;8:3834–8.
  32. Kumar R, Nyk M, Ohulchanskyy TY, Flask CA, Prasad PN. Combined optical and MR bioimaging using rare earth ion doped NaYF<sub>4</sub> nanocrystals. *Adv Funct Mater.* 2009;19:853–9.
  33. Chen G, Ohulchanskyy TY, Law WC, Agren H, Prasad PN. Monodisperse NaYbF<sub>4</sub>: Tm<sup>3+</sup>/NaGdF<sub>4</sub> core/shell nanocrystals with near-infrared to near-infrared upconversion photoluminescence and magnetic resonance properties. *Nanoscale.* 2011;3:2003–8.
  34. Zhou J, Sun Y, Du X, Xiong L, Hu H, Li F. Dual-modality in vivo imaging using rare-earth nanocrystals with near-infrared to near-infrared (NIR-to-NIR) upconversion luminescence and magnetic resonance properties. *Biomaterials.* 2010;31:3287–95.
  35. Troyan SL, Kianzad V, Gibbs-Strauss SL, Gioux S, Matsui A, Oketokoun R, Ngo L, Khamene A, Azar F, Frangioni JV. The FLARE intraoperative near-infrared fluorescence imaging system: a first-in-human clinical trial in breast cancer sentinel lymph node mapping. *Ann Surg Oncol.* 2009;16:2943–52.
  36. Vahrmeijer AL, Frangioni JV. Seeing the invisible during surgery. *Br J Surg.* 2011;98:749–50.
  37. Soga K, Tokuzen K, Tsuji K, Yamano T, Hyodo H, Kishimoto H. NIR bioimaging: development of liposome-encapsulated, rare-earth-doped Y<sub>2</sub>O<sub>3</sub> nanoparticles as fluorescent probes. *Eur J Inorg Chem.* 2010;18:2673–7.
  38. Hemmer E, Yamano T, Kishimoto H, Soga K. Gadolinium-containing inorganic nanostructures for biomedical applications: cytotoxic aspects. In: IEEE Explore, proceedings of the international conference on nanoscience and nanotechnology (ICONN), Sydney, Australia; 2010. p. 225–9.
  39. Singh S, Bhat MK. Carboplatin induces apoptotic cell death through downregulation of constitutively active nuclear factor- $\kappa$ B in human HPV-18 E6-positive Hep-2 cells. *Biochem Biophys Res Commun.* 2004;318:346–53.
  40. Farrer RA, Butterfield FL, Chen VW, Fourkas JT. Highly efficient multiphoton-absorption-induced luminescence from gold nanoparticles. *Nano Lett.* 2005;5:1139–42.
  41. Matijevic E, Hsu WP. Preparation and properties of monodispersed colloidal particles of lanthanide compounds. *J Colloid Interface Sci.* 1987;118:506–23.
  42. Park IY, Kim D, Lee J, Lee SH, Kim KJ. Effects of urea concentration and reaction temperature on morphology of gadolinium compounds prepared by homogeneous precipitation. *Mater Chem Phys.* 2007;106:149–57.
  43. Wang Y, Bai X, Liu T, Dong B, Xu L, Liu Q, Song H. Solvothermal synthesis and luminescence properties of monodisperse Gd<sub>2</sub>O<sub>3</sub>:Eu<sup>3+</sup> and Gd<sub>2</sub>O<sub>3</sub>:Eu<sup>3+</sup>@SiO<sub>2</sub> nanospheres. *J Solid State Chem.* 2010;183:2779–85.
  44. Mu Q, Chen T, Wang Y. Synthesis, characterization and photoluminescence of lanthanum hydroxide nanorods by a simple route at room temperature. *Nanotechnology.* 2009;20:345602.
  45. Lin S, Dong X, Jia R, Yuan Y. Controllable synthesis and luminescence property of LnPO<sub>4</sub> (Ln = La, Gd, Y) nanocrystals. *J Mater Sci Mater Electron.* 2010;21:38–44.
  46. Du G, Van Tendeloo G. Preparation and structure analysis of Gd(OH)<sub>3</sub> nanorods. *Nanotechnology.* 2005;16:595–7.
  47. Wang X, Li Y. Synthesis and characterization of lanthanide hydroxide single-crystal nanowires. *Angew Chem Int Ed.* 2002;41:4790–3.
  48. Wang X, Li Y. Solution-based routes to transition-metal oxide one-dimensional nanostructures. *Pure Appl Chem.* 2006;78:45–64.
  49. Ma L, Chen WX, Zhao J, Zheng YF. Synthesis of Pr(OH)<sub>3</sub> and Pr<sub>6</sub>O<sub>11</sub> nanorods by microwave-assisted method: effects of concentration of alkali and microwave heating time. *J Cryst Growth.* 2007;303:590–6.
  50. Venkatachalam N, Saito Y, Soga K. Synthesis of Er<sup>3+</sup> doped Y<sub>2</sub>O<sub>3</sub> nanophosphors. *J Am Ceram Soc.* 2009;92:1006–10.
  51. Günther A, Bender P, Birringer R. Rotational diffusion of magnetic nickel nanorods in colloidal dispersions. *J Phys Condens Matter.* 2011;23:325103.
  52. Mahler H-C, Jiskoot W. Analysis of aggregates and particles in protein pharmaceuticals. Hoboken: Wiley; 2012. p. 44.
  53. Soga K, Okumura Y, Tsuji K, Venkatachalam N. Effect of K<sub>3</sub>PO<sub>4</sub> addition as sintering inhibitor during calcination of Y<sub>2</sub>O<sub>3</sub> nanoparticles. *J Phys Conf Ser.* 2009;191:012003.
  54. Wang X, Li Y. Rare-earth-compound nanowires, nanotubes, and fullerene-like nanoparticles: synthesis, characterization, and properties. *Chem Eur J.* 2003;9:5627–35.

55. Hemmer E, Yamano T, Kishimoto H, Soga K. Cytotoxicity of  $Gd_2O_3:Ln^{3+}$  nanostructures and their potential as biomarkers. In: Meyer G, editor. Proceedings of the 7th international conference on f elements, ICfE-7, Terrae Rarae; 2009. p. 1–10.
56. Dong Y, Feng SS. Methoxy poly(ethylene glycol)-poly(lactide) (MPEG-PLA) nanoparticles for controlled delivery of anticancer drugs. *Biomaterials*. 2004;25:2843–9.
57. Xie J, Xu C, Kohler N, Hou Y, Sun S. Controlled PEGylation of monodisperse  $Fe_3O_4$  nanoparticles for reduced non-specific uptake by macrophage cells. *Adv Mater*. 2007;19:3163–6.
58. Sheng Y, Yuan Y, Liu C, Tao X, Shan X, Xu F. In vitro macrophage uptake and in vivo biodistribution of PLA-PEG nanoparticles loaded with hemoglobin as blood substitutes: effect of PEG content. *J Mater Sci Mater Med*. 2009;20:188–891.
59. Bazile D, Prud'Homme C, Bassoullet MT, Marlard M, Spenlehauer G, Veillard M. Stealth Me.PEG-PLA nanoparticles avoid uptake by the mononuclear phagocytes system. *J Pharm Sci*. 1995;84:493–8.
60. Wu H, Liu G, Zhuang Y, Wu D, Zhang H, Yang H, Hu H, Yang S. The behavior after intravenous injection in mice of multiwalled carbon nanotube/ $Fe_3O_4$  hybrid MRI contrast agents. *Biomaterials*. 2011;32:4867–76.
61. Al Faraj A, Fauvelle F, Luciani N, Lacroix G, Levy M, Crémillieux Y, Canet-Soulas E. In vivo biodistribution and biological impact of injected carbon nanotubes using magnetic resonance techniques. *Int J Nanomed*. 2011;6:351–61.
62. Tasciotti E, Godin B, Martinez JO, Chiappini C, Bhavane R, Liu X, Ferrari M. Near-infrared imaging method for the in vivo assessment of the biodistribution of nanoporous silicon particles. *Mol Imaging*. 2011;10:56–68.
63. Gratton SEA, Williams S, Napier ME, Pohlhaus PD, Zhou Z, Wiles KB, Maynor BW, Shen C, Olafsen T, Samulski ET, DeSimone JM. The pursuit of a scalable nanofabrication platform for the use in material and life science applications. *Acc Chem Res*. 2008;41:1685–95.
64. Sadauskas E, Wallin H, Stoltenberg M, Vogel U, Doering P, Larsen A, Danscher G. Kupffer cells are central in the removal of nanoparticles from the organism. *Particle Fibre Toxicol*. 2007;4:10.
65. Kryza D, Taleb J, Janier M, Marmuse L, Miladi I, Bonazza P, Louis C, Perriat P, Roux S, Tillement O, Billotey C. Biodistribution study of nanometric hybrid gadolinium oxide particles as a multimodal SPECT/MR/optical imaging and theragnostic agent. *Bioconjug Chem*. 2011;22:1145–52.
66. Tu C, Ma X, House A, Kauzlarich SM, Louie AY. PET imaging and biodistribution of silicon quantum dots in mice. *ACS Med Chem Lett*. 2011;2:285–8.
67. Nagayama S, Ogawara K, Fukuoka Y, Higaki K, Kimura T. Time-dependent changes in opsonin amount associated on nanoparticles alter their hepatic uptake characteristics. *Int J Pharm*. 2007;342:215–21.
68. Arnida, Janát-Amsbury MM, Ray A, Peterson CM, Ghandehari H. Geometry and surface characteristics of gold nanoparticles influence their biodistribution and uptake by macrophages. *Eur J Pharm Biopharm*. 2011;77:417–23.